communications physics

A Nature Portfolio journal

Article

https://doi.org/10.1038/s42005-025-02337-1

Multistate control of nonlinear photocurrents in ferroelectric IV-monochalcogenide monolayers via phase manipulation of the light field

Ali Kazempour[1,2], Esmaeil Taghizadeh Sisakht[2], Mahmut Sait Okyay[3], Xiao Jiang[2], Shunsuke Sato[4], Jinseok Oh[2] & Noejung Park[2]

Ultrafast optical control of ferroelectricity using short, intense light pulses enables precise manipulation of ferroelectric materials, offering potential breakthroughs in nonvolatile memory technologies. We demonstrate that phase manipulation of electric fields in the strong-field sub-cycle regime induces nonlinear injection currents that couple efficiently with band topology, dynamically reversing both current and polarization. Time-dependent first-principles calculations show that tuning the phase of linearly or circularly polarized light-via chirp or carrier-envelope phase-breaks time-reversal symmetry, allowing control over multi-ferroelectric states. In SnTe monolayers, nonlinear coupling between current and band topology enables dynamic ferroelectric manipulation. Time- and momentum-resolved transverse current analysis highlights the role of Berry curvature multipoles, linking odd/even orders to pseudo-harmonics that drive polarization reversal. These phase manipulations of short pulse waveforms may lead to control of nonlinear photocurrents and polarization states, paving the way for precise ultrafast opto-ferroelectric devices.

Ferroelectric materials, characterized by their spontaneous electric polarization that can be reversed by a bias, have recently gained significant interest, particularly for potential technological applications[1–7]. In recent years, the exploration of opto-ferroelectric properties has opened new avenues for manipulating electronic polarization at ultrafast timescales[8,9]. The interaction of these materials with ultrashort and ultrastrong laser pulses allows high-speed generation of non-equilibrium carriers, leading to polarization dynamics, polarization switching, and domain evolution[9,10]. Such a high-speed accurate control of ferroelectric polarization may give rise to new functionalities in the fields of non-volatile memory elements, sensors, or transducers[4,11].

Among two dimensional (2D) ferroelectric structures, optical control of polarization switching[8,12] is of particular interest, and recent studies have shown promising advancements in this area, especially in group IV monochalcogenides[13]. In SnTe monolayers, researchers have demonstrated reversible optical control of in-plane ferroelectric polarization using linearly polarized light. The mechanism was shown to involve the selective excitation of optical phonon modes in the terahertz regime that couple to the ferroelectric order parameter[14]. Theoretical studies combining group theory and first-principles calculations have shown that intrinsic in-plane ferroelectricity in materials like GeS monolayers can induce spontaneous valley polarization, leading to the electrical control of ferrovalley states. The unique electronic characteristics of group-IV monochalcogenides are thought to enable the development of electrically tunable polarizers, leading to the generation of linearly or even circularly polarized light[15]. Moreover, the inherent non-centrosymmetric nature of ferroelectric materials makes them ideal platform for nonlinear optical studies such as second harmonic generation and shift currents[16–19]. Recent studies[20] have introduced the photon helicity as a tool to control photogalvanic charge and spin currents via a ferroelectricity-driven adjustment of Berry curvature dipole (BCD), eventually leading to polarization reversal. For example, Wang et al. revealed that ferroelastic switching flips nonlinear shift and circular photocurrents by ±90°, while ferroelectric switching induces a 180° flip. Switching light polarization between left and right circular also flips circular photocurrent by 180°[21]. Among the monochalcogenide class, SnTe has attracted the most wide interest. Monolayer SnTe exhibits strong in-plane ferroelectricity[22] and

[1]Department of physics, Payame Noor University, 119395-3697, Tehran, Iran. [2]Department of Physics, Ulsan National Institute of Science and Technology (UNIST), Ulsan, Republic of Korea. [3]Materials Science and Engineering Program, Department of Chemical and Environmental Engineering, University of California-Riverside, Riverside, CA, USA. [4]Center for Computational Sciences, University of Tsukuba, Tsukuba, Japan. e-mail: noejung@unist.ac.kr

significant Berry curvature effects due to their non-centrosymmetric structure[19], which facilitate pronounced nonlinear optical responses. This property is essential not only for achieving effective control over polarization states but also underpins the principles of the nonlinear Hall effect (NLHE) making them highly sensitive to external phase modulation of light. This sensitivity, combined with their direct band gap and robust spin-orbit coupling (SOC), positions SnTe as an ideal candidate for exploring the dynamic control of electronic states, offering potential advancements in ultrafast optoelectronic devices.

A particularly promising approach involves manipulating chirp parameters and the carrier-envelope phase (ϕ_{CEP}) for pulse shaping, which advantageously allows precise controls over electronic states transition[23,24] together with efficient excitation of nonlinear phonons through optimized pulse shaping[25]. ϕ_{chirp} modulates timing and intensity, aiding polarization reversal, while ϕ_{CEP} affects the symmetry and amplitude of the induced polarization. It has been shown that[26,27] the residual current in graphene can be reversed by changing the ϕ_{CEP}, attributed to Landau-Zener-Stückelberg (LZS) interference. Residual current refers to the remaining current after the laser pulse ends, capturing the net displacement of charge carriers during the pulse duration. Additionally, the complex ϕ_{CEP} dependence of solid harmonics, influenced by tunneling and multiphoton ionization, underscores the nuanced control achievable through ϕ_{CEP} manipulation[28]. These insights advance ultrafast optoelectronics and tailored experimental designs. In this study, we investigate the interaction of phase-modulated short pulses with ferroelectric monolayer SnTe. Our findings demonstrate that manipulating the phase of light through techniques such as chirp and ϕ_{CEP} serves as a critical control parameter for ferroelectricity-driven nonlinear photocurrent switching. Both chirp and ϕ_{CEP} break time-reversal symmetry, enabling the residual current to reveal the characteristics as nonlinear injection currents. We discuss the second-order residual transverse current and its reversal, which scales with the dynamical polarization and modulates the Berry curvature and its multipoles induced by chirped pulses.Unlike previous studies on CEP- and chirp-controlled photocurrents in 2D materials such as graphene, TMDCs, and topological insulators[29,30], our work uniquely focuses on monolayer SnTe- as an example of noncentrosymmetric ferroelectrics with a switchable in-plane polarization. Using real-time TDDFT simulations, we reveal highly anisotropic and switchable photocurrent dynamics governed by material specific symmetry breaking and nonlinear excitation under tailored light fields.

Results

Geometry and electronic structure of monolayer SnTe

The monolayer SnTe features a staggered arrangement of tin (Sn) and tellurium (Te) atoms within a puckered rectangular lattice, characteristic of its structure, as depicted in Fig. 1a. This monolayer belongs to the Pmn21 space group and exhibits in-plane ferroelectricity, making it structurally similar to the puckered form of phosphorene. In this configuration, Sn and Te atoms shift in opposite directions along the [010] axis (the y-axis in Fig. 1a), results in broken inversion symmetry ($\mathcal{P}$), thereby contributing to its unique electronic properties and spontaneous polarization. This structure exhibits glide G and mirror M_{yz} plane symmetries as shown in Fig. 1a. These symmetries play a crucial role in shaping quantum geometry and nonlinear optical properties by imposing constrains on Berry curvature, enabling processes such as giant second harmonic generation[13,18,20,31]. The ferroelectric polarization in the monolayer SnTe results in two distinct structural states, P_y and P_{-y}, where the displacement of Sn and Te atoms along the [010] axis leads to polarization in opposite directions. The difference between these states lies in the direction of atomic displacement, which alters the electronic distribution and stabilizes one polarization state over the other depending on external conditions, such as strain or electric fields. When the ferroelectric polarization aligns with the armchair y-axis, the electronic structure of the monolayer SnTe reveals two valleys near the X and Y points in the Brillouin zone (BZ), henceforth referred to as the X and Y valleys. It is worth noting that although the monolayer SnTe structure adopts an orthorhombic lattice and lacks fourfold rotational symmetry, the calculated band structure without SOC appears nearly symmetric along the specified high-symmetry paths. This apparent symmetry arises from the small in-plane lattice anisotropy (~1.95%)[32], which results in similar orbital hybridization and hopping amplitudes along the two directions. Consequently, while the X and Y valleys are crystallographically inequivalent, they are electronically similar. Indeed, a closer inspection reveals that the X and Y valleys are not exactly identical (see the zoomed-in inset in Fig. 1c), and this subtle anisotropy becomes more pronounced when SOC is included (see Supplementary Material). The monolayer SnTe behaves as a semiconductor with an indirect band gap of 0.7 eV (Fig. 1c), as calculated using density functional theory (DFT). The valence band maximum and conduction band minimum occur at distinct points along the ΓX and ΓY lines, respectively. The distinctive band structure around these valley points is responsible for the observed giant shift-current conductivities[19].

Multistate control of nonlinear photocurrents by phase shaping

We begin by calculating the evolution of current responses over time when exposed to a two-cycle short pulse with a constant carrier-envelope phase (ϕ_{CEP}) and a time-varying ϕ_{chirp}. The driver field is defined as $\boldsymbol{E}(t) = E_0 f(t)\cos(\omega t + \phi(t))\hat{\boldsymbol{e}}$ where for chirped pulse $\phi(t) = \phi_{chirp} = bt^2$, while for a CEP-stabilized pulse, $\phi(t) = \phi_{CEP}$ is constant. Before making comparisons, we briefly explain the behavior of the pulse with ϕ_{chirp} and ϕ_{CEP}. The ϕ_{CEP} which is the phase offset between the peak of the envelope and the phase of the carrier wave is time-independent. It allows the precise control of the electric field on a sub-cycle basis, which is crucial for the coherent control of electron dynamics in few-cycle pulses. Conversely, the ϕ_{chirp} refers to a time-dependent gradient in phase that controls the frequency content of the pulse over time, influencing the timing and spectral properties of the interaction. The symmetry of the pulse is partially disrupted by chirping, so the positive and negative parts are no longer identical. For instance, the acceleration caused by the interaction of an electron with the negative part of the oscillation is not canceled by the

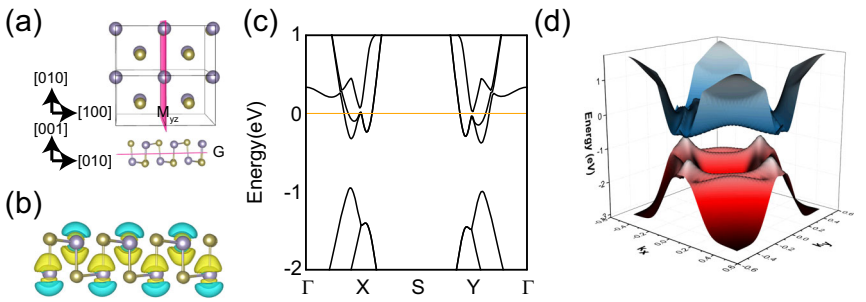

Fig. 1 | Structural geometry, charge density, and electronic structure of the monolayer SnTe. a Top and side views of the monolayer SnTe. Displacement along the y-axis between Sn (olive green) and Te (violet) induces in-plane ferroelectricity along the y direction. **b** Side view of the charge density difference between the ferroelectric phase and the reference paraelectric phase. Yellow/Cyan isosurfaces represent positive/negative charge distribution, with positive values showing increased electron density and negative values showing decreased electron density. **c**, **d** Two-dimensional and three-dimensional band structures, respectively, showing the inequivalent X and Y valleys.

deceleration from the interaction with the corresponding positive part. As a result, there is a net acceleration, or equivalently, a net energy gain by the electron from the pulse. We emphasize that the polarization dynamics discussed here arise solely from the electronic component, as the sub-cycle timescales of the laser pulses preclude ionic motion.

Figure 2a illustrates a typical comparison of Ponderomotive energy ($U_p = \alpha E^2/\omega^2$, where α is proportionality constant) variation over one cycle for an input frequency of 1.55 eV with ϕ_{chirp} and ϕ_{CEP} at an intensity of 10^{13} Wcm^{-2}. The relationship between the Ponderomotive energy and the Keldysh parameter (γ), defined as ($\gamma = \sqrt{\frac{I_p}{2U_p}}$,) where I_p is ionization potential, offers a quantitative method to differentiate multiphoton mechanism from the tunneling ionization mechanisms[33,34]. This relationship indicates that phase modulation can influence the relative contributions of these two ionization processes. Thus, a higher U_p favors tunneling ionization, where intraband dynamics of electrons affect interband transitions[26,28]. Therefore, the relative magnitude of Ponderomotive energy gained by an electron under a linearly chirped laser alters both interband and intraband transition dynamics, making them much more complex compared to a ϕ_{CEP} modulated laser. Further, it should be noted that, while keeping the ionic energy fixed during the calculation, the energy of both configurations with equilibrium spontaneous polarizations P_{+y} and P_{-y} becomes unequal and lose balance after exposure to both unchirped and chirped irradiation. This destabilizes the double well potential surface, decreases the depth of the well, and leads to polarization reversal, which will be discussed later.

Figure 2b shows vector potential time-profile and the induced current response for linearly polarized pulses with unchirped/chirped and $\phi_{CEP} = 0$, π phases. The time-dependent Kohn-Sham equation for the electron dynamics and the definitions of the cell-averaged and momentum-resolved current are described in the "Method" section. We first align the electric field along the in-plane spontaneous polarization direction [010] and the driving field is active only during the first two periods of oscillation and is turned off after the second period. The chirp phase is chosen linear and must change the sign of the vector potential before it reaches zero, i.e., the vector potential of light field having a nonzero time integral. As the driving fields for lasers in unchirped/chirped and $\phi_{CEP} = 0$, π phases are in the strong nonlinear regimes, the total currents resemble the laser shape with a small phase lag between the peaks of the current and the applied pulse. Increasing the incident frequency tends to reduce the phase delay. When the laser is turned off after the two-cycle operation, the current remains finite and almost constant as we neglect temperature and charge relaxation. due to remanent polarization, which is referred to as residual current in what follows. This dc residual current at sufficiently large field remains finite due to higher-order nonlinear process contribution[35]. Noticeably, the residual current induced by chirped light is opposite to unchirped light, as shown in Fig. 2b (upper right panel). The reversal of residual current is also observed when the ϕ_{CEP} of the applied field changes from 0 to π, as shown in Fig. 2b (bottom right panel). In the Supplementary material we have shown that a sequential reversal of residual current occurs as a function of chirp rate for both positive and negative values, provided that the vector potential changes sign before being switched off. Breaking the time-reversal symmetry

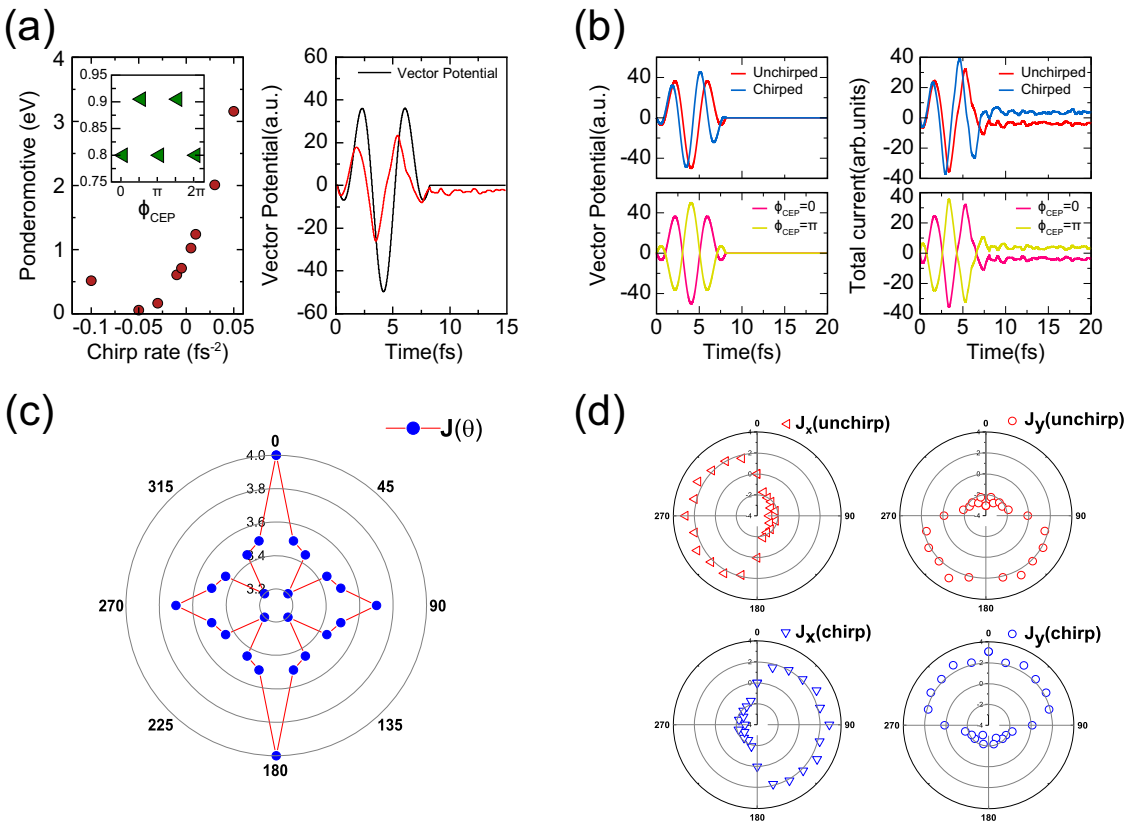

Fig. 2 | Residual current dynamics induced by chirped and CEP phase-modulated pulses. a Ponderomotive energy, defined as the average kinetic energy gained by electrons in a laser field, is shown as a function of constant ϕ_{CEP} and time-varying ϕ_{chirp}. The pulse fluence corresponding to different chirp rates ranges from 0.015 to 0.085 a.u. The changing frequency in the chirp case, modified the group velocity of electrons (the velocity associated with wave packet dynamics in k-space), resulting in a non-uniform induced current. (left). The phase delay of the current(red) relative to the applied field (black) is depicted (right). **b** The top (bottom) panel shows the total current comparison between unchirped ($\phi_{CEP} = 0$) and chirped ($\phi_{CEP}=\pi$) conditions. The residual current in the chirped case ($\phi_{CEP} = \pi$) is reversed compared to the unchirped case ($\phi_{CEP} = 0$) when the laser ends. **c** Full polarimetry of the residual current magnitude for unchirped case. θ is the angle between electric field of pulse and the spontaneous polarization. **d** The top (bottom) panel compares the transverse and longitudinal residual current components for unchirped (red) and chirped (blue) conditions, clearly showing the current direction reversal.

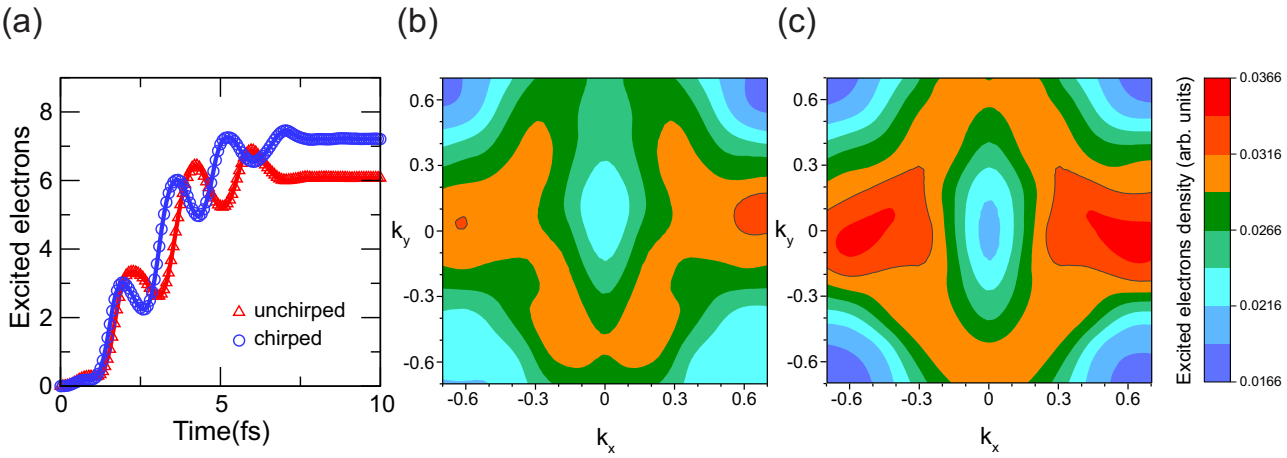

Fig. 3 | Dynamics of excited electrons and population imbalance. a The evolution of excited electron numbers in the conduction band over time for both unchirped (red) and chirped (blue) pulse conditions. The chirped pulse induces a higher population of excited electrons due to phase modulation effects, leading to an imbalance that enhances the residual current. **b**, **c** The distribution of *k*-resolved electron population within the first Brillouin zone (BZ) for unchirped and chirped fields, respectively.

between Kramers pairs in the BZ using the chirp parameter induces a population imbalance. Referenced to the chirp-free light, those positive chirp rates b that generate a greater than an odd number but less than the next even number lead to a reversed current.

The full polarimetry profile of the total current, along with its longitudinal and transverse components for both unchirped and chirped lasers, is illustrated in Fig. 2c, d. A transverse current ($J_\perp$) is generated alongside the longitudinal current ($J_\parallel$) at all incident angles, except for $\theta = 0$ and $\theta = \pi$, which correspond to the orientation of the spontaneous polarization. Both residual $J_\perp$ and $J_\parallel$ currents show a reversal after the laser pulse ends. The symmetry of mirror M_{yz} and also a two-fold rotation (C_{2v}) is clearly recovered from the polar plot of the total current. The C_{2v} symmetry imposes constraints $\chi^{(2)}_{ijk} = -\chi^{(2)}_{jik}$ for $i \neq j$ on the nonlinear optical tensors such as second-order susceptibility $\chi^{(2)}$. The transverse component, which we show in the next section to be a second-order current, suggest that the spontaneous polarization, normalized to its static equilibrium value $P_s(\tau)/P_s(0)$, undergoes reversal in these transient regimes. More importantly, we will later address how ferroelectricity is dominantly affected by the electric field induced Berry curvature[36,37]. Symmetry breaking or reduction, induced by chirp modulation of the phase, manifests in optical responses through the involvement of both odd and even order derivatives of the Berry curvature.

Notably, selecting chirp rates b of equal magnitude but opposite signs in applied electric field in the form of $\boldsymbol{E}(t) = E_0 f(t)\cos(\omega t + bt^2)\hat{\boldsymbol{e}}$ results in distinct residual currents, differing both in strength and direction, as illustrated in the Supplementary Material. This occurs because $\pm b$ produce different frequency spectra over the vector potential. We also present calculations for unchirped and chirped setups over a larger number of cycles, including the effects of pumped IR-active phonons in the structure, which amplify the dynamical polarizations. All calculations demonstrate a reversal in the direction of residual currents, provided the system remains in the short-pulse regime, where both time-reversal $\mathcal{T}$ and inversion symmetries $\mathcal{P}$ are broken, though the magnitude of the residual current may vary. Furthermore, we observe that scattering mechanisms, such as phonons, do not significantly alter the overall outcome. For instance, we explored the enhancement of in-plane polarization via nonlinear phonon pumping, as described in ref. 31, and found that introducing out-of-plane A_u and in-plane E_u phonons does not impact the general trend. Notably, this residual current reversal is robust, persisting for up to 250 fs within the framework of Ehrenfest dynamics, even in the presence of ionic motion (see Supplementary Material Note 4).

In both unchirped and chirped pulses, the longitudinal ($J_\parallel$) and transverse ($J_\perp$) currents exhibit reversal. This sign change induces a π polarization rotation, with similar current reversals expected for constant ϕ_{CEP} values of 0 and π. A parallel phenomenon occurs in LZS interference in graphene[26], where the current direction depends on the ϕ_{CEP}. The ϕ_{CEP} modulates electron trajectory lengths in reciprocal space, shifting interference from constructive to destructive due to population imbalances. This ϕ_{CEP} dependent interference explains the photocurrent's sensitivity to ϕ_{CEP} in graphene under few-cycle pulses.

As shown in Fig. 2b, the time-reversal symmetry $\mathcal{T}$ of the vector potential is broken in the case of chirped pulses with a carrier-envelope phase (ϕ_{CEP}) of π, where $\boldsymbol{A}(t) \neq \boldsymbol{A}(-t)$. This symmetry breaking in the vector potential leads to a time-reversal symmetry violation in the Hamiltonian, resulting in a population imbalance and a residual current.The current reversal arises from two distinct mechanisms: chirp modulation (top panel) creates directional asymmetry through spectrally imbalanced carrier excitation across the pulse duration. while CEP inversion (bottom panel) flips the residual current via sub-cycle quantum interference. Figure 3a, b, c present a comparison of the number of excited electrons over time and the resulting population imbalance across the BZ for both unchirped and chirped pulses. We attribute the observed population imbalance in the unchirped case to the intrinsic breaking of inversion symmetry within the system, which we trace back to the relaxation of accumulated polarization. This initial imbalance differs from the induced imbalance in the population during the aforementioned phases. Notably, the chirped pulse excites an additional electron into the conduction band compared to the unchirped case, leading to a distribution that initially favors the $-k_x$ valley at lower intensities but extends to other regions beyond the valleys in the strong-field regime. Additionally, as demonstrated in the Supplementary Information, chirp rates that generated number of excited electrons is between an odd and the next even integer reverse the direction of the current compared to that induced by an unchirped field. It is worth noting that the incident time of the interaction is short enough, allowing the system to remain below the damage threshold despite the presence of a large number of excited electrons.

While earlier studies have largely explored the connection between current direction, ferroelectricity, and the Berry curvature poles in monolayer SnTe[20,21], our findings here provide a clearer perspective. We show that the reversibility of ferroelectric polarization-closely tied to current reversal through a sign change in Berry curvature-can be precisely controlled. This control is achieved by adjusting the population imbalance between the left and right valleys, which is governed by the handedness of circularly polarized light[20,21].

Chirp-driven time-reversal breaking and persistent injection current

Sato et al.[35,38] investigated the limitations of mean-field methods, such as TD-Hartree, TD-Hartree-Fock, and TDDFT, in capturing second-order shift and injection currents. These mean-field approximations can result in unphysical DC responses, even after the system is exposed to linearly polarized light. This occurs due to population imbalances between k and $-k$ states (Kramers pairs) in the BZ. Such imbalances are thought to arise quantum interference incurred on artificial self-excitation pathways, which are absent in exact many-body treatments. In TDDFT, such unphysical part of the residual current are attributed to time-nonlocal memory effects which can be mitigated by improving the exchange-correlation kernel $f_{Hxc}(r, r', \omega)$. Using a many-body Schrödinger framework, the study identified three key factors contributing to population imbalance: the vector potential, its interference with the induced mean-field potential, and the induced mean-field potential itself. Under time-reversal symmetry, these contributions cancel out; however, chirped laser pulses break this symmetry, leading to a real, physical injection current that persists after the pulse ends. Injection current now refers specifically to the second-order photocurrent arising from velocity mismatch of carriers in valence and conduction band due to asymmetric excitation of carriers in momentum space[39,40].

Furthermore, the introduction of a chirp imposes distinct phase shifts across pulse components, leading to quasi-phase matching that enhances quantum interference between excitation pathways[41]. This mechanism can result in a more pronounced and stable residual current, in contrast to scenarios where time-reversal symmetry $\mathcal{T}$ remains preserved. We highlight that both the magnitude and direction of the induced dc current are highly sensitive to the specific properties of the chirped pulse, such as the chirp rate and the overall temporal profile.

Recently, the mechanisms underlying the generation of shift and injection currents under various material symmetries and light polarizations have been investigated[42]. It was demonstrated that in systems with broken $\mathcal{P}$, $\mathcal{T}$, and $\mathcal{PT}$ symmetries, both shift and injection currents can be produced simultaneously under LPL and CPL irradiation. Our findings confirm that introducing a chirp phase offers a framework that facilitates the concurrent generation of shift and injection currents. However, we identify that the residual current is an injection current, oriented orthogonally to the spontaneous polarization direction[43]. The shift current also contribute to second order transverse current. The symmetry property of shift current susceptibility is governed by point group and permutation symmetry, which correspond to direct product $\Gamma_i \otimes \Gamma_E \otimes \Gamma_E$. In monolayer group IV monochalcogenides with C_{2v} point group (see Table S1 for the character table of C_{2v}), for transverse component of the shift current $J^y_{SC} = \sigma^{yxx} E_x E_x$, we have $\Gamma_{j_y} \otimes \Gamma_{E_x} \otimes \Gamma_{E_x} = A_1 \otimes B_2 \otimes B_2 = A_1$. It contains totally symmetric representation A_1 indicating that the shift current can be induced along y under LPL in the x direction. While the introduction of a chirp modifies the excitation of charge carriers across various energy levels, the injection current remains perpendicular to the polarization. This occurs because the chirped pulse affects the occupation of states within BZ without inducing strain or altering electronic structure.

Origin of chirp-induced current and polarization switching

The fundamental characteristics and switching dynamics of shift and injection currents in group-IV monochalcogenide monolayers are determined by the interplay between symmetries, shift vectors, and Berry curvature[21,44–46]. For instance, the ferroelectric properties, essential for modulating the Berry curvature and other nonlinear optical responses, are significantly influenced by the helicity of incident circular light and the resultant photogalvanic current[20]. Moreover, in time-reversal symmetric metallic systems, the NLHE arises as a second-order response to external electric fields which is attributable to the BCD. This corresponds to the lowest-order non-vanishing effects of band geometries contributing to charge transport properties at the Fermi surface[47]. Furthermore, the second-order harmonic generation resulting from transverse nonlinear optical responses in a $\mathcal{T}$-preserved insulator bears resemblance to the nonlinear Hall effect (NLHE) observed in metallic systems as both phenomena stem from the breaking of inversion symmetry and involve the generation of a transverse response that is quadratic in the applied field, thus bridging the gap between optical and electronic nonlinear effects in disparate material platforms[48]. As the incident field intensity increases, multipoles of the Berry curvature become more pronounced. These terms, representing more intricate asymmetries in momentum space, grow increasingly important under stronger perturbations. When an external electric field excites additional electrons into the conduction band, the Fermi level rises, rendering the system more metallic in nature. We show that applying a chirped pulse offers an effective way to unveil the interplay of aforementioned factors by incorporating both odd and even orders of Berry curvature multipoles through the breaking of $\mathcal{T}$ symmetry. The obtained results can be explained in terms of interband Berry curvature, as described by ref. 48. In the presence of a phase-modulated strong field given by $\boldsymbol{E}(t) = E_0\,\mathrm{Re}[e^{i\Phi(t)}]\hat{\boldsymbol{x}}$, where $\Phi(t) = \omega t + \phi(t)$, we introduce the step function $\Theta(\Phi(t) - \omega_{nm})$ to account for all states that satisfy the gap frequency condition $\Phi(t) \geq \omega_{nm}$ where n and m are valence and conduction bands. In the strong-field regime, the anomalous velocities arising from both the valence and conduction bands are governed by the total Berry curvature of the system. This can be expressed in terms of the total interband Berry curvature $\Omega_{nm}(\boldsymbol{k})$[48].

Using the corresponding vector potantial $\boldsymbol{A}(t) = \frac{-cE_0}{\Phi'(t)} Im[e^{i\Phi(t)}]\hat{\boldsymbol{x}}$, the phase-dependent Bloch oscillation of carriers is written as $\Delta k = \frac{-eE_0}{\hbar\Phi'(t)} Im[e^{i\Phi(t)}]$. This can be transferred to the interband Berry curvature and consequently, the transverse current is given by:

$$\mathbf{J}_\perp(t) = 2\frac{e^2}{\hbar}\mathbf{E}(t) \times \sum_{nm} \int \frac{d^2\mathbf{k}}{4\pi^2} \Omega_{nm}(\mathbf{k} + \Delta k\hat{x})\Theta(\Phi(t) - \omega_{mn}(\mathbf{k})). \quad (1)$$

Depending on the form of phase $\Phi(t)$, the phase-modulated strong field can either preserve the $\mathcal{T}$ symmetry or break it. In former case, as we show in Supplementary material, the transverse current $\mathbf{J}_\perp(t)$ is determined by the odd order derivatives of interband Berry curvature and as a result we revealed the interrelationship between even-order psudo-harmonics $\Phi(t)$ and series of even-order interband Berry curvature multipoles $\mathbf{D}^{(2p)}_{nm}(\Phi) = \int_{\mathbf{k}} \frac{\partial^{(2p-1)}\Omega_{nm}}{\partial \mathbf{k}^{(2p-1)}} \Theta(\Phi - \omega_{nm})$ as following

$$\mathbf{J}_\perp(t) = \sum_{p=even,\geq 2} \sum_{q\geq p} \mathrm{Im}[e^{ip\Phi}] \frac{\alpha_q E_0^q}{\Phi'^{(q-1)}} D^{(q)} \quad (2)$$

Here, we take α_q as constant coefficients and Φ' is time-derivative of phase. In addition, the above results show how different even-order nonlinear responses contribute to the transverse current. It is worth noting that if we consider the weak field limit in which the interband transition is dominant within effective two-band model, the above generalized equation is reduced to well-known second-order response of $\mathbf{J}_\perp(t) \propto \hat{z} \times \boldsymbol{E}(\boldsymbol{D}^{(2)}_{nm} \cdot \boldsymbol{E})$[47]. On the other hand, when $\mathcal{T}$ is broken the transverse current is given by (see Supplementary material)

$$\begin{aligned}\mathbf{J}_\perp(t) = &\sum_{p=odd,\geq 1} \sum_{q\geq p} \mathrm{Re}[e^{ip\Phi}] \frac{\alpha_q E_0^q}{\Phi'^{q-1}} D^{(q)} \\ &+ \sum_{p=even,\geq 2} \sum_{q\geq p} \mathrm{Im}[e^{ip\Phi}] \frac{\alpha_q E_0^q}{\Phi'^{q-1}} D^{(q)}.\end{aligned} \quad (3)$$

This compact formulation illustrates that the transverse current is comprised of a mixture of even and odd orders of interband Berry curvature multipoles. Additionally, the equation indicates the coupling of odd (even) orders of Berry curvature multipoles to odd (even) pseudo-harmonics. Further, the Fourier transform of the current $\mathbf{J}_\perp(t)$ reveals

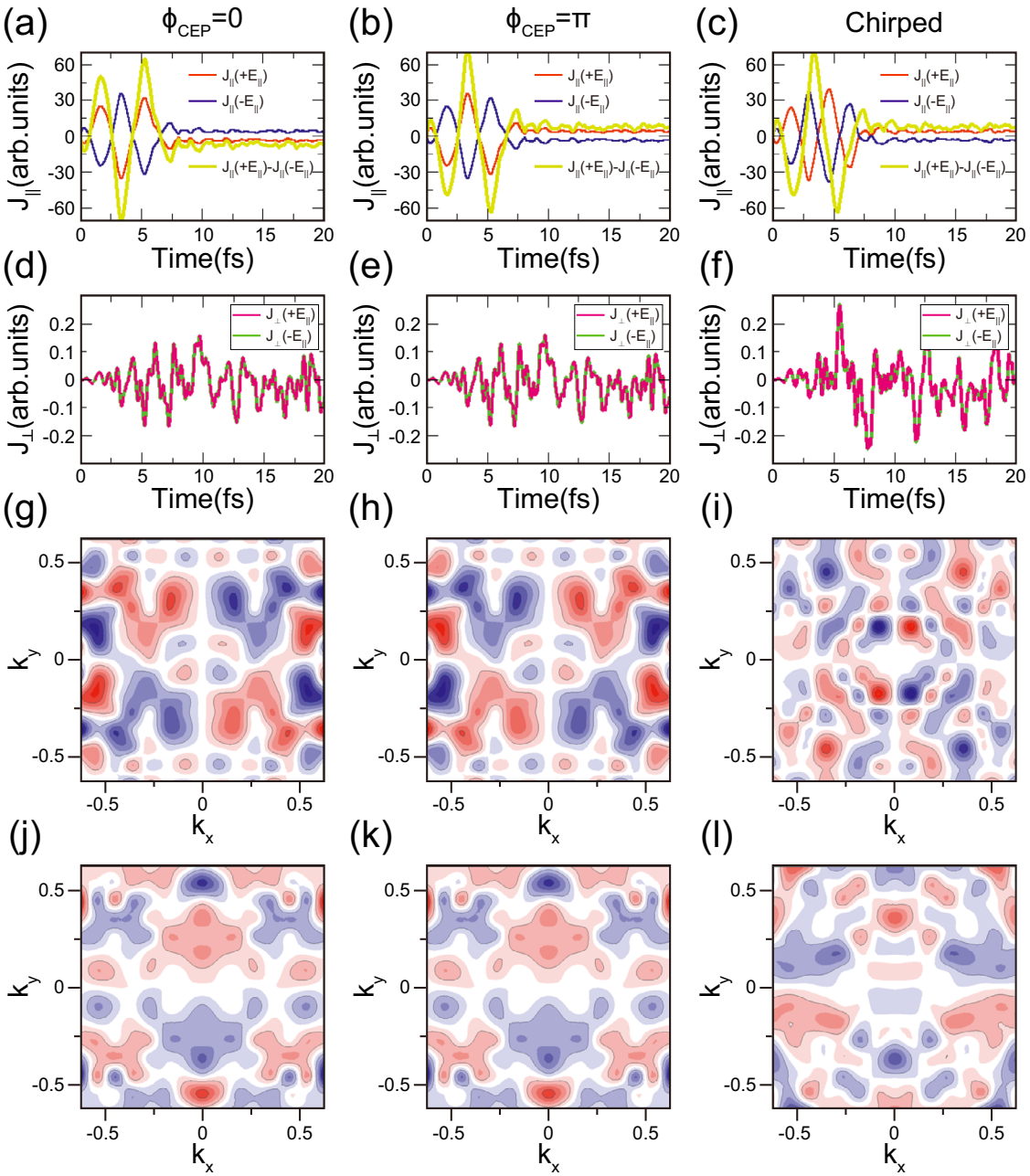

Fig. 4 | Time and momentum-resolved profile of currents from chirp and CEP modulation. a–c Time-resolved profiles of longitudinal currents $J_{\parallel}$(induced current parallel to electric field) and **d–f** transverse currents $J_{\perp}$ (induced current perpendicular to electric field) under opposite electric fields $\mp E$ for unchirped (chirped) pulses and carrier-envelope phase ϕ_{CEP} values of 0 (π). The transverse current $J_{\perp}$ does not change sign when the electric is reversed, indicating that it arises from a second-order nonlinear response. **g–i** Show a comparison of the momentum-resolved distribution of j^{A} at ϕ_{CEP} values of 0 and π and chirped pulse. The k-resolved j^{A} exhibits odd parity of higher poles in the Berry curvature with respect to the mirror plane, when the current is reversed from $\phi_{CEP} = 0$ to π and chirped. **j-l** correspond to the k-resolved j^{Σ}, as discussed in the text, which highlights the even-order poles of the Berry curvature.

that the current consists of both even and odd harmonics with a phase delay of $\pi/2$. The above equations (2), (3) and the associated arguments are particularly well-suited and valid for few-pulse dynamics induced by irradiation with sufficiently long pulses. Transitioning to short-pulse, subcycle dynamics likely breaks $\mathcal{T}$-symmetry, as the short pulses are generally asymmetric in time. Therefore, in our study, we restrict the use of equation (3) to all phase-modulated cases. In light of this, $D^{(q)}$ for even (odd) q must undergo transformation according to even (odd) parity by reversing the sign of $+E$ to $-E$, ensuring that $\mathbf{J}_{\perp}(t)$ does not change sign. This result aligns with the findings of Ye et al.[36], which demonstrate that the polarization direction of the Berry curvature is affected by the relative orientation of the electric field and the crystal axis. Notably, the Berry curvature direction can be reversed by changing the polarity of the DC field. Figures 4d-f depict the comparison between the transverse current under $\pm E\hat{\boldsymbol{x}}$ for ϕ_{CEP} of 0, π, and chirped pulse, respectively. Notably, the current for a ϕ_{CEP} of π remains comparable to that for $\phi_{CEP} = 0$, consistent with the summation described in Eq. (3). Furthermore, the current under a chirped pulse, where the chirp phase further breaks time-reversal symmetry $\mathcal{T}$, enhances the contribution from odd-order multipoles and harmonics. Extending the contribution beyond the BCD in enhanced nonlinear anomalous Hall effects due to $\mathcal{T}$ breaking is consistent with previous work[49]. We then obtain the real-time sum and

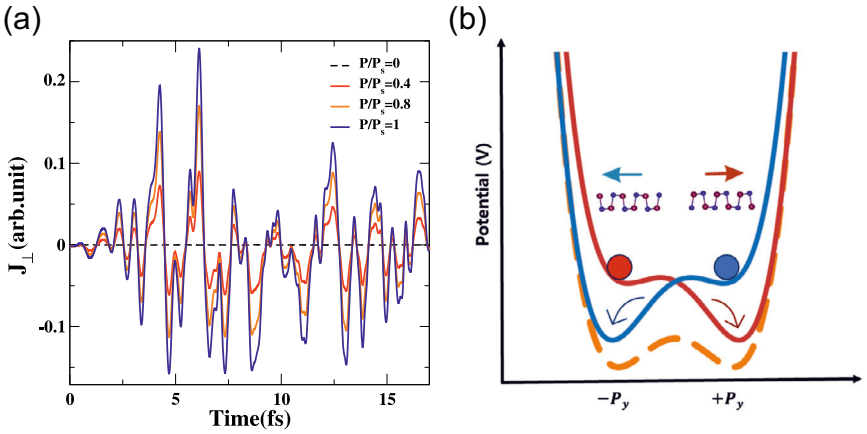

Fig. 5 | Transverse current and chirped pulse effects on ferroelectric PES. a The transverse current magnitude increases as higher-order contributions from the Berry curvature become more prominent, responding to the ferroelectric polarization strength. The polarization (P) scales from zero in the non-polar paraelectric phase to a maximum value (P_s) when the material reaches full ferroelectric polarization. **b** The schematic shows how a chirped laser pulse changes the double-well electronic potential energy surface (PES) of a ferroelectric material. The red curve represents the original (unchirped) PES, while the blue curve shows the modified (chirped) PES, creating an asymmetry. This asymmetry causes a electronic polarization reversal from P_{+y} to P_{-y} after the laser is turned off. The orange curve represents the unperturbed PES.

difference of transverse currents as follows:

$$\mathbf{J}^{\Delta}(t) = \frac{J_{\perp}^{E} - J_{\perp}^{-E}}{2} = 0, \tag{4}$$

and

$$\mathbf{J}^{\Sigma}(t) = \frac{J_{\perp}^{E} + J_{\perp}^{-E}}{2} = \sum_{p=\text{odd},\geq 1} \sum_{q\geq p} \mathrm{Re}\left[e^{ip\Phi}\right] \frac{\alpha_q E_0^q}{\Phi'^{q-1}} D^{(q)} + \sum_{p=\text{even},\geq 2} \sum_{q\geq p} \mathrm{Im}\left[e^{ip\Phi}\right] \frac{E_0^q}{\Phi'^{q-1}} D^{(q)}, \tag{5}$$

We can attribute these real time sum and difference currents to an effective k-resolved density current as $\mathbf{J}^{\Sigma(\Delta)}(t) = \int_k d\mathbf{k}\mathbf{j}^{\Sigma(\Delta)}(t,k)$. The k-resolved density current directly mirrors the distribution of Berry curvature in momentum space, with regions of high current intensity corresponding to areas of significant Berry curvature[50,51]. In Supplementary Materials Note 5, the analysis of k-resolved density currents $\mathbf{j}^{\Sigma(\Delta)}(t)$ under low-intensity linear and high-intensity nonlinear fields reveals that the X and Y valleys contribute predominantly in the weak field regime, while under strong fields, the entire BZ becomes involved in the current. Figures 4g-l illustrate these momentum-resolved density currents $\mathbf{j}^{(\Delta)}(t)$ and $\mathbf{j}^{\Sigma}(t)$ at the moment the laser is turned off. Comparing the $\mathbf{j}^{(\Delta)}(t)$ for unchirped($\phi_{CEP}=0$) with $\phi_{CEP}=\pi$ shows mirror-image opposites distribution coming from odd parity $D^{(q)}$ with odd q in Eq.(3). At low intensities, the odd parity term $D^{(1)}$ corresponds to Ω_{nm}, while in the high-intensity regime, higher-order terms such as $\frac{\partial^2\Omega}{\partial k^2}$ also become relevant. This holds true even in the chirped case (see Fig. 4l). The k-resolved distribution of the density $\mathbf{j}^{(\Delta)}(t)$ is somewhat different for $\phi_{CEP}=\pi$, as the chirped parameter further breaks time-reversal symmetry $\mathcal{T}$ and increases the frequency, making the occupation frequency-dependent. Nevertheless, odd parity terms $D^{(q)}$, such as the Berry curvature and its even derivatives, remain responsible for current and polarization reversal. As expected from the comparison of Fig. 4j, k, the current $\mathbf{j}^{(\Sigma)}(t)$ reflects the even-parity $D^{(q)}$ terms, which remain unchanged under a reversal of the electric field sign.

Furthermore, to investigate the interplay between polarization and topology, we computed the transverse currents for varying magnitudes of ferroelectric polarization, ranging from 0 (the paraelectric phase) to 1 (the maximum ferroelectric phase), as illustrated in Fig. 5a. As shown, the enhancement of the transverse current is directly scaled and amplified with increasing polarization magnitude, driven by its correlation with the Berry curvature and its higher-order multipole components. These results emphasize the crucial role of ferroelectricity-induced topological effects in governing nonlinear optical responses, and highlight the significant contribution of higher-order Berry curvature terms to the observed current behavior. The double-well potential maps the energy profile of varying polarization strengths, offering insights into polarization switching and stable polarization directions along the ferroelectric mode. Under laser exposure, this potential is modified, revealing dynamic behavior. For an unchirped pulse, symmetry between the wells is disrupted, stabilizing the $+P_y$ well over the $-P_y$ one. A chirped pulse reverses this preference, favoring the $-P_y$ well as shown in Fig. 5b[14,52,53]. Both pulse types lower the barrier height between wells, facilitating polarization transitions. This dynamic switching between $\pm P_y$ states, driven by the pulse type, offers a pathway for binary data storage, with stable polarization states representing 0 and 1 for future electronic devices.

Multibit ferroelectricity polarization control by chirp and handedness

We now compare the current induced by the unchirped and chirped circularly polarized pulses, as illustrated in Fig. 6a, b. As expected, changing the handedness from left-handed circular polarization (LCP) to right-handed circular polarization (RCP) reverses the direction of the residual current components. Specifically, J_x switches from negative to positive, while J_y consistently remains negative. However, for chirped circularly polarized light (CPL), reversing the polarization from LCP to RCP results in J_y always being positive, with J_x changing sign from negative to positive. This comparison highlights that, while the total residual current undergoes a $\frac{\pi}{2}$ rotation when switching between unchirped LCP and RCP, introducing a chirp phase to CPL induces an additional $\frac{\pi}{2}$ rotation relative to the unchirped case. This combined effect of light helicity and chirp phase enables the realization of four distinct ferroelectricity states corresponding to four well potential picture, as schematically illustrated in Fig. 6d, compared to linearly polarized light that supports only two states, corresponding to a π rotation in the current and polarization direction. The four-well potential describes an energy landscape with four distinct minima, each corresponding to a unique in-plane ferroelectric polarization state, which arise from the four possible directions of residual current in the x-y plane, controlled by combinations of light handedness and chirp parameters.

A previous study[21] demonstrated a π-phase shift in the current direction under both linearly and circularly polarized light for shift and injection currents. In contrast, when coupled with ferroelastic transitions along the x- or y-axis of a monolayer, both shift and injection currents undergo a 90° rotation under the same polarization conditions. In this work, we show that chirping the pulse breaks time-reversal symmetry $\mathcal{T}$, enabling the residual current to dictate the direction of the injection current. Consequently, similar to the findings of the earlier study, linearly polarized chirped light results in a 180° reversal of both the shift current and the residual injection

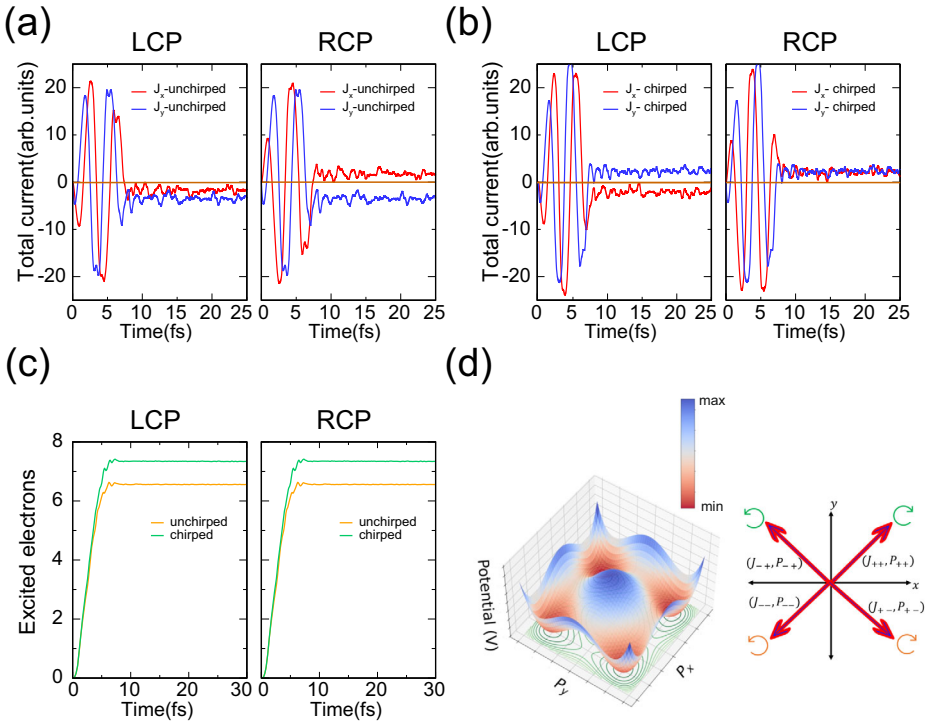

Fig. 6 | Chirp-modulated phase effects in circularly polarized light. a, **b** show the effect of the chirp-modulated phase in circularly polarized light with right and left handedness, respectively, as compared to the unchirped case. **c** Shows the electron population excited into the conduction band for both unchirped and chirped pulses of left and right circular polarization. **d** Schematic representation of the four-well transient electronic potential picture arising from the combined effects of chirped pulses and light helicity. The diagram illustrates how left- and right-handed circularly polarized light (LCP and RCP), when modulated with or without chirp, lead to four distinct ferroelectric states. Current states $\mathbf{J}_{\alpha\beta}$ (α: x, β: y components) correspond to polarization directions $\mathbf{P}_{\alpha\beta}$. Orange/green arrows denote unchirped/chirped pulses combined with light helicity (↻/↺).

current. However, chirped circularly polarized light induces a 90° rotation of the total residual currents, accompanied by a 90° reversal in polarization.

Discussion

In our study, we investigated the phase modulation of strong-field, short-duration pulses in the nonlinear photocurrent responses of 2D ferroelectric monolayer SnTe. By applying a time-varying chirp and constant carrier-envelope phase (ϕ_{CEP}) offset, we observed significant imbalance of population within the BZ as a function of the chirp rate. Notably, we found a directional reversal of the residual current upon removal of the laser field. This current reversal was observed for both chirped and constant CEP phase-modulated light, irrespective to its linear or circular polarization. Importantly, this reversal of the injection current was accompanied by a concomitant rotation in the polarization direction.

Time-resolved analysis of injection currents, as a function of the incident angle of irradiation, indicates that the chirp parameter can effectively control the direction of polarization by modifying the regional occupation weight across the BZ. Additionally, the k-resolved second-order transverse current scales with the Berry curvature even and odd-order poles and pseudo-harmonics in strong-field regimes. As the external electric field dynamically modulates the ferroelectric polarization, these higher-order Berry curvature moments contribute to complex nonlinear optical phenomena such as higher harmonic generation and nonlinear Hall effects. Moreover, exploiting the circularly polarized driver, both through the manipulation of chirp parameter or handedness of the circular driver, we can effectively adjust the time-reversal symmetry $\mathcal{T}$ of the system, leading to non-equivalent interactions with the electronic states. This results in ferroelectricity multi-states with distinct current and polarization characteristics. This interaction enhances the sensitivity of polarization dynamics to external stimuli, particularly to sub-laser-cycle dynamics, potentially improving the material's nonvolatile memory capabilities through the coupling of electronic states and ferroelectric order. We anticipate that the observed reversal and rotation of current and polarization, driven by ϕ_{chirp} or ϕ_{CEP} modulation, could be applicable to group-IV monochalcogenide monolayers due to their similar electronic and atomic structures. These findings suggest potential extensions beyond monolayer SnTe, offering new strategies for phase-controlled nonlinear optics in other 2D materials and broadening the scope of ultrafast optoelectronic applications. Unlike previous studies that focused primarily on static field effects, our work demonstrates dynamic manipulation of photocurrents and polarization, providing a more versatile approach to ferroelectric control.

In our study, we investigate the phase manipulation of light fields as a means to control nonlinear photocurrents in ferroelectric materials, using time-dependent density functional theory (TDDFT) within the adiabatic local-density approximation (ALDA), augmented by gradient-corrected exchange-correlation functionals. Although many-body correlations are not explicitly treated in this mean-field approach, it has been shown to qualitatively capture key features of shift and injection currents-such as their symmetry properties, polarization dependence, and sensitivity to laser parameters[38]. A more accurate theoretical framework, explicitly incorporating many-body interactions and improved exchange-correlation kernels, may yield quantitatively refined results, but such an extension is beyond the scope of the present study.

Eventually, to address the role of decoherence and dissipation, we explicitly include the effects of phonon pumping and ionic relaxation. These additional channels provide insight into how environmental interactions can influence the persistence of multistate control. Our results indicate that while such dissipative processes can modify the residual current, signatures of multistate behavior remain robust within experimentally relevant parameter regimes. While our work demonstrates ultrafast control of electronic polarization through tailored light fields, practical memory applications would require future studies of coupled electron-lattice dynamics to establish switching metrics such as retention time and coercive fields under optical excitation.

Methods

Our calculations utilize time-dependent density functional theory (TDDFT) to model the time-evolution of the wave function and electronic current within the ALDA, as implemented in the real-space, real-time framework via the OCTOPUS code[54–56]. We examine electron dynamics under the influence of both linearly and circularly polarized laser pulses, incorporating either a time-dependent chirp parameter or a constant carrier-envelope phase ϕ_{CEP}. The electrons dynamics are captured by solving the

time-dependent Kohn-Sham equations in the velocity gauge.

$$i\hbar\frac{\partial\phi_n(r,t)}{\partial t}=\left\{\frac{1}{2m}\left[-i\hbar\nabla+\frac{e}{c}\boldsymbol{A}(t)\right]^2+V_{ion}(r,t)+\int dr'\frac{e^2}{|r-r'|}\rho(r',t)+V_{xc}(r,t)\right\}\phi_n(r,t), \tag{6}$$

where $\boldsymbol{A}(t)$ represents the time-dependent profile of the vector potential, which is written as

$$\boldsymbol{A}=A_0 f(t)\cos(\omega t+\Phi)\hat{\boldsymbol{e}} \tag{7}$$

Here, $f(t)$ represents the envelope function (in our case we considered cosinoidal envelope centered at $t=t_0$, lasting from $t_0-\tau_0$ to $t_0+\tau_0$), ω denotes the driver frequency, and $\hat{e}$ specifies the polarization vector, which can be either linearly or circularly polarized. It is important to note that for very short pulses, as considered in this work, the pulse envelope f(t) with cosine shape can change significantly within a single period. To prevent unphysical results, the vector potential should be designed to vanish as $(t\rightarrow\pm\infty)$. Note that in our pulse the envelope f(t) has compact support and vanishes smoothly at the pulse edges, thereby guaranteeing that the time-integrated electric field over the entire pulse duration is zero[57]. The phase Φ of the electric waveform is tailored to support two pulse-shaping methods: a dynamic phase characterized by a linear chirp, $\Phi_{chirp}=bt^2$ with b ranging from $[0.01, 0.1]\,\mathrm{fs}^{-2}$, and a constant carrier-envelope phase ϕ_{CEP}, which introduces a phase offset between the carrier wave and the pulse envelope. Both Φ_{chirp} and ϕ_{CEP} laser modulation break time-reversal symmetry, thereby altering the electric field profile within the pulse.

We set the strong intensity $I=10^{13}\mathrm{Wcm}^{-2}$ for incident pulse with the duration of two cycles, ensuring the sub-cycle dynamics. The chirp parameter sensitivity is analyzed in Supplementary Note 3, where we show that the pulse duration remains effectively constant across different chirp values, consistent with the fixed envelope used in our simulations (see Fig. S3). We clarify that the octopus code implementation applies a quadratic phase to the carrier wave while keeping the pulse envelope and duration fixed, resulting in changes to fluence and peak intensity but preserving the overall fluence range, thereby modeling chirp without pulse broadening. To address experimental feasibility, we estimate the damage threshold of SnTe monolayers to be $\sim(0.5-1)\times10^{13}\,\mathrm{W\,cm}^{-2}$ for femtosecond pulses, consistent with trends observed in SnSe and related structures[58]. While our TDDFT simulations predict nonthermal lattice dynamics, experimental realization would require pulse durations <100 fs to avoid thermal damage, as carrier lifetimes in SnTe monolayers are expected to be sub-picosecond due to strong electron-phonon coupling[59]. The driving frequency was set to $\omega=1.55$ eV, which surpasses the band gap and corresponds to one of the prominent peaks in the shift current spectra[19]. Ionic motion and phonon excitation are fully frozen in the present work under the assumption that the pulse durations are on the order of femtoseconds, significantly shorter than typical lattice dynamics response times. We minimally tested the effects of phonon, by exciting A_u and E_u infrared-active modes. Though the phonons contribute to the amplifications of polarization dynamics, (see Supplementary Materials Note 4), they do not fundamentally alter the current reversal behavior with which we are mainly concerned in the present work. It is important to note that the lattice's ionic component lacks sufficient time to respond to these extremely short pulses.

The real-space grid is sampled with a spacing of 0.35 Bohr, and the k-point mesh for the 2D BZ is uniformly set to $24\times24\times1$ based on convergence tests. The momentum-resolved current density within the unit cell is calculated as:

$$\mathbf{j}(t,k)=\sum_n\frac{1}{\Omega}Re\left[\int d\mathbf{r}\phi^*_{nk}(r,t)\hat{\mathbf{v}}\phi_{nk}(r,t)\right] \tag{8}$$

The average electric current density over the entire BZ is then given by:

$$\mathbf{J}(t)=\sum_k\sum_n\frac{1}{\Omega}Re\left[\int d\mathbf{r}\phi^*_{nk}(r,t)\hat{\mathbf{v}}\phi_{nk}(r,t)\right] \tag{9}$$

where $\hat{\mathbf{v}}=\frac{1}{m_e}\left(-i\hbar\nabla+\frac{e}{c}\mathbf{A}\right)$ is the velocity operator, and Ω represents the unit cell volume.

The number of excited electrons N_{ex} in the conduction band is obtained as:

$$N_{ex}(t)=\sum_k\sum_{n=n_{occ}+1}^{\infty}\sum_{m=1}^{n_{occ}}\left|\left\langle\phi_{m,k}(t>0)|\phi_{n,k}(t=0)\right\rangle\right|^2 \tag{10}$$

where n is the band index and k is the Bloch number, respectively.

Data availability

The data that support the findings of this study are available from the corresponding author upon reasonable request.

Received: 13 April 2025; Accepted: 29 September 2025;
Published online: 17 November 2025

References

1. Bian, R. et al. Developing fatigue-resistant ferroelectrics using interlayer sliding switching. *Science* **385**, 57–62 (2024).
2. Wang, S. et al. Two-dimensional ferroelectric channel transistors integrating ultra-fast memory and neural computing. *Nat. Commun.* **12**, 53 (2021).
3. Kim, T. Y., Kim, S. K. & Kim, S.-W. Application of ferroelectric materials for improving output power of energy harvesters. *Nano Converg.* **5**, 30 (2018).
4. Scott, J. F. & Paz de Araujo, C. A. Ferroelectric memories. *Science* **246**, 1400–1405 (1989).
5. Qi, L., Ruan, S. & Zeng, Y.-J. Review on recent developments in 2d ferroelectrics: theories and applications. *Adv. Mater.* **33**, 2005098 (2021).
6. Gao, Y., Gao, M. & Lu, Y. Two-dimensional multiferroics. *Nanoscale* **13**, 19324–19340 (2021).
7. Barraza-Lopez, S., Fregoso, B. M., Villanova, J. W., Parkin, S. S. & Chang, K. Colloquium: physical properties of group-iv monochalcogenide monolayers. *Rev. Mod. Phys.* **93**, 011001 (2021).
8. Guo, J. et al. Recent progress in optical control of ferroelectric polarization. *Adv. Opt. Mater.* **9**, 2002146 (2021).
9. Yang, M.-M. & Alexe, M. Light-induced reversible control of ferroelectric polarization in bifeo3. *Adv. Mater.* **30**, 1704908 (2018).
10. Lian, C., Ali, Z. A., Kwon, H. & Wong, B. M. Indirect but efficient: laser-excited electrons can drive ultrafast polarization switching in ferroelectric materials. *J. Phys. Chem. Lett.* **10**, 3402–3407 (2019).
11. Guo, R. et al. Non-volatile memory based on the ferroelectric photovoltaic effect. *Nat. Commun.* **4**, 1990 (2013).
12. Guan, Z. et al. Recent progress in two-dimensional ferroelectric materials. *Adv. Electron. Mater.* **6**, 1900818 (2020).
13. Fei, R., Kang, W. & Yang, L. Ferroelectricity and phase transitions in monolayer group-IV monochalcogenides. *Phys. Rev. Lett.* **117**, 097601 (2016).
14. Zhou, J. & Zhang, S. Terahertz optics-driven phase transition in two-dimensional multiferroics. *npj 2D Mater. Appl.* **5**, 16 (2021).
15. Shen, X.-W., Tong, W.-Y., Gong, S.-J. & Duan, C.-G. Electrically tunable polarizer based on 2d orthorhombic ferrovalley materials. *2D Mater.* **5**, 011001 (2017).
16. Rangel, T. et al. Large bulk photovoltaic effect and spontaneous polarization of single-layer monochalcogenides. *Phys. Rev. Lett.* **119**, 067402 (2017).

17. Orenstein, J. et al. Topology and symmetry of quantum materials via nonlinear optical responses. *Annu. Rev. Condens. Matter Phys.* **12**, 247–272 (2021).
18. Wang, H. & Qian, X. Giant optical second harmonic generation in two-dimensional multiferroics. *Nano Lett.* **17**, 5027–5034 (2017).
19. Jin, G. & He, L. Peculiar band geometry induced giant shift current in ferroelectric snte monolayer. *npj Comput. Mater.* **10**, 23 (2024).
20. Kim, J. et al. Prediction of ferroelectricity-driven berry curvature enabling charge-and spin-controllable photocurrent in tin telluride monolayers. *Nat. Commun.* **10**, 3965 (2019).
21. Wang, H. & Qian, X. Ferroicity-driven nonlinear photocurrent switching in time-reversal invariant ferroic materials. *Sci. Adv.* **5**, eaav9743 (2019).
22. Chang, K. et al. Discovery of robust in-plane ferroelectricity in atomic-thick snte. *Science* **353**, 274–278 (2016).
23. Neyra, E. et al. High-order harmonic generation driven by chirped laser pulses induced by linear and non linear phenomena. *Eur. Phys. J. D.* **70**, 1–6 (2016).
24. Astapenko, V. & Romadanovskii, M. Excitation of a two-level system by a chirped laser pulse. *Laser Phys.* **19**, 969–973 (2009).
25. Itin, A. & Katsnelson, M. Efficient excitation of nonlinear phonons via chirped pulses: Induced structural phase transitions. *Phys. Rev. B* **97**, 184304 (2018).
26. Higuchi, T., Heide, C., Ullmann, K., Weber, H. B. & Hommelhoff, P. Light-field-driven currents in graphene. *Nature* **550**, 224–228 (2017).
27. Zhang, X., Du, H., Wang, W., Guo, H. & Liu, C. Residual current under the combined effect of carrier envelope phase and chirp: phase shift and peak enhancement. *Opt. Express* **31**, 26879–26887 (2023).
28. Wang, H. et al. Complex carrier-envelope-phase effect of solid harmonics under nonadiabatic conditions. *Phys. Rev. A* **99**, 023406 (2019).
29. Rana, N. & Dixit, G. Optical control of ultrafast photocurrent in graphene. *Phys. Rev. B* **110**, 054105 (2024).
30. Quereda, J. et al. Symmetry regimes for circular photocurrents in monolayer mose2. *Nat. Commun.* **9**, 3346 (2018).
31. Shin, D. et al. Dynamical amplification of electric polarization through nonlinear phononics in 2d snte. *npj Comput. Mater.* **6**, 182 (2020).
32. Wan, W., Liu, C., Xiao, W. & Yao, Y. Promising ferroelectricity in 2D group IV tellurides: a first-principles study. *Appl. Phys. Lett.* **111**, 132904 (2017).
33. Kruchinin, S. Y., Krausz, F. & Yakovlev, V. S. Colloquium: strong-field phenomena in periodic systems. *Rev. Mod. Phys.* **90**, 021002 (2018).
34. Kazempour, A., Morshedloo, T. & Wang, F. Transient non-linear optics of diamond under ultrashort excitation pulses. *Appl. Phys. A* **127**, 1–10 (2021).
35. Mao, W., Rubio, A. & Sato, S. A. Nonlinear current injection in hexagonal boron nitride using linearly polarized light in a deeply off-resonant regime. *Adv. Opt. Mater.* **12**, 2400651 (2024).
36. Ye, X.-G. et al. Control over Berry curvature dipole with electric field in WTe 2. *Phys. Rev. Lett.* **130**, 016301 (2023).
37. Lai, S. et al. Third-order nonlinear Hall effect induced by the Berry-connection polarizability tensor. *Nat. Nanotechnol.* **16**, 869–873 (2021).
38. Sato, S. A. & Rubio, A. Limitations of mean-field approximations in describing shift-current and injection-current in materials. *Phys. Rev. B* **109**, 195205 (2024).
39. Sipe, J. & Shkrebtii, A. Second-order optical response in semiconductors. *Phys. Rev. B* **61**, 5337 (2000).
40. Young, S. M. & Rappe, A. M. First principles calculation of the shift current photovoltaic effect in ferroelectrics. *Phys. Rev. Lett.* **109**, 116601 (2012).
41. Kovács, K., Balogh, E., Hebling, J., Toşa, V. & Varjú, K. Quasi-phase-matching high-harmonic radiation using chirped THz pulses. *Phys. Rev. Lett.* **108**, 193903 (2012).
42. Xu, H., Wang, H., Zhou, J. & Li, J. Pure spin photocurrent in non-centrosymmetric crystals: bulk spin photovoltaic effect. *Nat. Commun.* **12**, 4330 (2021).
43. Panday, S. R., Barraza-Lopez, S., Rangel, T. & Fregoso, B. M. Injection current in ferroelectric group-iv monochalcogenide monolayers. *Phys. Rev. B* **100**, 195305 (2019).
44. Fregoso, B. M., Morimoto, T. & Moore, J. E. Quantitative relationship between polarization differences and the zone-averaged shift photocurrent. *Phys. Rev. B* **96**, 075421 (2017).
45. Morimoto, T. & Nagaosa, N. Topological nature of nonlinear optical effects in solids. *Sci. Adv.* **2**, e1501524 (2016).
46. Tan, L. Z. & Rappe, A. M. Enhancement of the bulk photovoltaic effect in topological insulators. *Phys. Rev. Lett.* **116**, 237402 (2016).
47. Sodemann, I. & Fu, L. Quantum nonlinear Hall effect induced by Berry curvature dipole in time-reversal invariant materials. *Phys. Rev. Lett.* **115**, 216806 (2015).
48. Okyay, M. S. et al. Second harmonic Hall responses of insulators as a probe of Berry curvature dipole. *Commun. Phys.* **5**, 303 (2022).
49. Holder, T., Kaplan, D. & Yan, B. Consequences of time-reversal-symmetry breaking in the light-matter interaction: Berry curvature, quantum metric, and diabatic motion. *Phys. Rev. Res.* **2**, 033100 (2020).
50. Shin, D. et al. Unraveling materials Berry curvature and Chern numbers from real-time evolution of Bloch states. *Proc. Natl. Acad. Sci. USA* **116**, 4135–4140 (2019).
51. Luu, T. T. & Wörner, H. J. Measurement of the berry curvature of solids using high-harmonic spectroscopy. *Nat. Commun.* **9**, 916 (2018).
52. Abalmasov, V. A. Ultrafast reversal of the ferroelectric polarization by a midinfrared pulse. *Phys. Rev. B* **101**, 014102 (2020).
53. Hanakata, P. Z., Carvalho, A., Campbell, D. K. & Park, H. S. Polarization and valley switching in monolayer group-IV monochalcogenides. *Phys. Rev. B* **94**, 035304 (2016).
54. Andrade, X. et al. Real-space grids and the Octopus code as tools for the development of new simulation approaches for electronic systems. *Phys. Chem. Chem. Phys.* **17**, 31371–31396 (2015).
55. Castro, A. et al. Octopus: a tool for the application of time-dependent density functional theory. *Phys. Status Solidi (b)* **243**, 2465–2488 (2006).
56. Marques, M. A., Castro, A., Bertsch, G. F. & Rubio, A. octopus: a first-principles tool for excited electron–ion dynamics. *Comput. Phys. Commun.* **151**, 60–78 (2003).
57. Liu, C. & Nakajima, T. Anomalous ionization efficiency by few-cycle pulses in the multiphoton ionization regime. *Phys. Rev. A* **76**, 023416 (2007).
58. Huang, Y. et al. Observation of a novel lattice instability in ultrafast photoexcited SnSe. *Phys. Rev. X* **12**, 011029 (2022).
59. Ito, H. et al. Observation of unoccupied states of snte (111) using pump-probe ARPES measurement. *Phys. Rev. Res.* **2**, 043120 (2020).

Acknowledgements

This research was supported by the National Research Foundation of Korea (NRF) grant funded by the Korea government (MSIT) (No. RS-2023-00257666, RS-2023-00218799, RS-2023-00208825). It was also supported by Samsung Electronics Co. through the Industry-University Cooperation Project (IO221012-02835-01) and by the Korea Institute for Advancement of Technology (KIAT) through a grant funded by the Korea government (MOTIE) (P0023703, HRD Program for Industrial Innovation). Additionally, this work was supported by the Brain Pool program funded by the Ministry of Science and ICT through the National Research Foundation of Korea (RS-2023-00283963).

Author contributions

A.K. carried out ab initio TDDFT calculations, analyzed the data, and prepared the figures. A.K., E.T.S., and N.P. wrote the manuscript. E.T.S., N.P., X.J., S.S., M.S.O., and J.O. contributed to strengthening the

discussion. All authors analyzed the results and contributed to the final manuscript.

Competing interests
The authors declare no competing interests.

Additional information
Supplementary information The online version contains supplementary material available at https://doi.org/10.1038/s42005-025-02337-1.

Correspondence and requests for materials should be addressed to Noejung Park.

Peer review information *Communications Physics* Chengpu Liu and the other, anonymous, reviewer(s) for their contribution to the peer review of this work. A peer review file is available.